

# Superstructure Variation and Improved Cycling of Anion Redox Active Sodium Manganese Oxides Due to Doping by Iron

Xiaodong Qi, Langyuan Wu, Zhiwei Li, Yuxuan Xiang, Yunan Liu, Kangsheng Huang, Elias Yuval, Doron Aurbach,\* and Xiaogang Zhang\*

Anionic redox provides an effective way to overcome the capacity bottleneck of sodium-ion batteries. A dominant role is played by the arrangement of alkali A and transition metal M in the  $\text{Na}_x\text{A}_y\text{M}_{1-y}\text{O}_2$  superstructure. Here, in situ X-ray diffraction and ex situ  $^7\text{Li}$  nuclear magnetic resonance of P2 type  $\text{Na}_{0.6}\text{Li}_{0.2}\text{Mn}_{0.8}\text{O}_2$  with ribbon-ordered superstructure illustrate structural changes and explain the evolution of the electrochemical behavior of electrodes comprising this active mass, during cycling. Upon substitution of a small amount of manganese by iron,  $\text{Na}_{0.67}\text{Li}_{0.2}\text{Mn}_{0.73}\text{Fe}_{0.07}\text{O}_2$  is formed with a honeycomb-ordered superstructure. Experimental characterizations and theoretical calculations elucidate the effect of iron on oxygen redox activity. The iron-doped material considerably outperforms the undoped  $\text{Na}_{0.6}\text{Li}_{0.2}\text{Mn}_{0.8}\text{O}_2$  as a cathode material for rechargeable Na-ion batteries. This research reveals the effect of superstructure transformation on the electrochemical properties and offers a new perspective on element substitution in anionic redox active cathode materials.

## 1. Introduction


For the past decades, rechargeable lithium-ion batteries (LIBs) have conquered the market of portable electronic devices and

X. Qi, L. Wu, Z. Li, Y. Liu, K. Huang, X. Zhang  
Jiangsu Key Laboratory of Electrochemical Energy Storage Technologies  
College of Materials Science and Technology  
Nanjing University of Aeronautics and Astronautics  
Nanjing 210016, P. R. China  
E-mail: azhangxg@nuaa.edu.cn

L. Wu, E. Yuval, D. Aurbach  
Department of Chemistry and Institute of Nanotechnology & Advanced  
Materials (BINA)  
Bar-Ilan University  
Ramat-Gan 5290002, Israel  
E-mail: Doron.Aurbach@biu.ac.il

Y. X. Xiang  
School of Engineering  
Westlake University  
Hangzhou 557712, P. R. China

X. Zhang  
Key Laboratory for Intelligent Nano Materials and Devices  
of the Ministry of Education  
Nanjing University of Aeronautics and Astronautics  
Nanjing 210016, P. R. China

 The ORCID identification number(s) for the author(s) of this article can be found under <https://doi.org/10.1002/aenm.202202355>.

DOI: 10.1002/aenm.202202355

are becoming promising energy storage sources for transportation.<sup>[1–2]</sup> However, rising demand and intrinsic inhomogeneous distribution of lithium give rise to the price of raw materials of the LIBs.<sup>[3]</sup> In addition, the need for large-scale energy storage, calls for more cost-effective and sustainable electrode materials. Sodium-ion batteries (SIBs), due to the high abundance and wide distribution of sodium resources, as well as similar working principles as with LIBs, have drawn positive focus from battery companies and research institutions.<sup>[4]</sup> The inherent larger ionic radius of  $1.02 \text{ \AA}$  and heavier molar weight of  $\text{Na}^+$  over  $\text{Li}^+$  ions impose a penalty on the specific capacity of sodium-ion cathode materials, and the standard electrode potential of  $\text{Na}^+/\text{Na}$  is  $0.3 \text{ V}$  higher than that of  $\text{Li}^+/\text{Li}$ , resulting in a disadvantage in energy density compared to

LIBs.<sup>[5–6]</sup> However, for applications related to load leveling and large energy storage, SIBs remain very attractive.

Recently, lattice oxygen redox (LOR) in intercalation host materials which broke the conventional concept for charge compensation, gained significant attention as electrodes' materials with such activity could achieve extremely high specific capacity even beyond the conventional theoretical capacity of intercalation electrodes' materials.<sup>[7–8]</sup> Thus, a new paradigm of SIBs in which LOR reactions could participate in charge compensation has attracted enormous focus.<sup>[9–10]</sup> To figure out the nature of LOR activity, extensive research and simulation calculations have been devoted. The occurrence of LOR depends on the position of the transition metal (TM) ( $n$ ) $d$  bands and O  $2p$  bands with respect to the Fermi level ( $E_F$ ).<sup>[11–14]</sup> The traditional oxygen bands in low energy levels can be raised by appropriate methods to close to the  $E_F$ , such as the formation of  $\text{Na}-\text{O}-\text{Li}$  and  $\text{Na}-\text{O}-\text{Mg}$  coordination structures which have been proved widely, enabling the O  $2p$  orbits in weakly bonded or narrow nonbonding states (highly localized states). As the electrochemical cells are charged to certain voltages, the electron holes would be generated in the above-mentioned O  $2p$  orbits rather than in the TM-O antibonding states, which activates the oxygen redox capability.<sup>[13–14]</sup>

Among them, manganese-based sodium-ion layered cathodes with the presence of small amounts of lithium are mainstream classes.<sup>[15]</sup> In most  $\text{Na}_x\text{Li}_y\text{TM}_{1-y}\text{O}_2$ , lithium occupies the original TM sites, and an in-plane ordering where

the Li-ions are surrounded by six TM ions is formed. Yabuuchi et al.<sup>[16]</sup> have investigated the honeycomb superstructure of P2-type  $\text{Na}_{2/3}[\text{Li}_{1/6}\text{Mn}_{5/6}]\text{O}_2$ . They ascertained the stacking sequences of superstructure ordering along the c-axis as AB-type. Nazar et al.<sup>[17]</sup> performed a long-term cycling test on P2-type honeycomb superstructure  $\text{Na}_{0.6}\text{Li}_{0.2}\text{Mn}_{0.8}\text{O}_2$ . Owing to stable structure evolution revealed by in situ X-ray diffraction (XRD), cathodes comprising this material could still deliver up to  $\approx 190 \text{ mA h g}^{-1}$  after 100 cycles. Rong et al.<sup>[18]</sup> proved the oxygen redox behaviors in P2-type honeycomb superstructure  $\text{Na}_{0.72}[\text{Li}_{0.24}\text{Mn}_{0.76}]\text{O}_2$  by X-ray absorption spectroscopy and revealed a suppressed phase transition.

Although the mentioned materials with honeycomb superstructure characteristics could exhibit outstanding specific capacity and decent cycling stability, the voltage hysteresis and voltage decay caused by irreversible local structural transformations limit their discharge-specific energy.<sup>[19–23]</sup> Recently, Bruce and coworkers proposed a ribbon-ordered superstructure in  $\text{Na}_{0.6}\text{Li}_{0.2}\text{Mn}_{0.8}\text{O}_2$ ,<sup>[24]</sup> presenting -Li-4Mn-Li- sequences viewed along the [100] direction. They demonstrated that owing to the suppression of TM in-plane migration by the ribbon-ordered superstructure, the voltage hysteresis could be substantially lowered. Unfortunately, the initial 20 cycles of galvanostatic charge and discharge curves of electrodes comprising  $\text{Na}_{0.6}\text{Li}_{0.2}\text{Mn}_{0.8}\text{O}_2$  with ribbon-ordered superstructure exhibit dramatic changes accompanied with a rapid capacity decay, showing undesirable instability. Gu et al.<sup>[25]</sup> revealed the topological characteristics in the ribbon-ordered superstructure and confirmed the  $-\alpha\beta$  configuration in P2-type  $\text{Na}_{0.6}\text{Li}_{0.2}\text{Mn}_{0.8}\text{O}_2$  and  $-\alpha\gamma$  sequences in P3-structured  $\text{Na}_{0.6}\text{Li}_{0.2}\text{Mn}_{0.8}\text{O}_2$ . They revealed that the ribbon-ordered P2- $\text{Na}_{0.6}\text{Li}_{0.2}\text{Mn}_{0.8}\text{O}_2$  evolved gradually from  $-\alpha\beta$  stacks to  $-\alpha\gamma$  stacks during cycling and thought the transformation of local ordering sequences, could be responsible for the degradation of cycling performance. Furthermore, Sung et al. explored the phase transition of ribbon-ordered P2-type  $\text{Na}_{0.6}\text{Li}_{0.2}\text{Mn}_{0.8}\text{O}_2$  by in situ XRD.<sup>[26]</sup> A noteworthy two-phase reaction induced by LOR activity was confirmed and verified by density functional theory (DFT) calculations.

Despite the great efforts that have been devoted to shedding light on the  $-\alpha\beta$  ribbon-ordered structure and some progress that could be achieved, the long-term cycling performance of the  $-\alpha\beta$  ribbon-ordered  $\text{Na}_{0.6}\text{Li}_{0.2}\text{Mn}_{0.8}\text{O}_2$  could not be realized yet (as far as we know). Also, there are no related reports on the effect of other elements on Li/TM ordering arrangements in these systems. Here, we systematically investigated long-term electrochemical properties evolution in  $-\alpha\beta$  ribbon-ordered  $\text{Na}_{0.6}\text{Li}_{0.2}\text{Mn}_{0.8}\text{O}_2$  (denoted as NLMO). After a rapid capacity decay within the initial 20 cycles, it is surprising that subsequent discharge capacities increase gradually with further cycles and even recover to the initial state, while the capacity-voltage curves have changed a lot. The initial high voltage plateau disappears and the capacity-voltage curves turn into S-shaped curves. In situ XRD and ex situ  $^7\text{Li}$  nuclear magnetic resonance (NMR) reveal that NLMO undergoes a structure evolution during the initial high voltage platform, while a stable structure could be maintained during the S-shaped capacity-voltage curves. Moreover, adding iron to the material could inhibit the migration of lithium ions among the TM layers and sodium layers, as was confirmed by solid-state NMR.<sup>[27]</sup> Meanwhile, the presence of

Fe ions can facilitate the charge-transfer process.<sup>[28–30]</sup> Then, we designed  $\text{Na}_{0.67}\text{Li}_{0.2}\text{Mn}_{0.73}\text{Fe}_{0.07}\text{O}_2$  (labeled as NLMFO) by introducing a minor amount of iron into the NLMO precursor, obtaining a new cathode material by the same synthetic method of P2-NLMO. We find that by the introduction of iron, the resulting cathode material prefers to form a honeycomb-ordered superstructure, which could lower the total energy. Moreover, we demonstrated that the introduction of iron could enable much more lattice oxygen atoms to participate in charge compensation redox activity through quantification of capacity contribution from the iron atoms and DFT calculations. Overall, the findings improve cognition of  $-\alpha\beta$  ribbon-ordered structure and reveal the effect of iron introduction on local ordering arrangement and LOR activity of these important SIBs cathode materials.

## 2. Results and Discussion

### 2.1. Preparation and Structure of NLMO and NLMFO

The expected NLMO and NLMFO were both synthesized via solid-state reaction under  $\text{O}_2$  atmosphere, and the details can be seen in the “Materials synthesis” in Experimental Sections. Morphologies of the as-synthesized materials were revealed by Scanning Electron Microscopy (SEM). The well-defined crystallites with regular hexagonal features of NLMO are shown in **Figure 1A**; Figures S1A, and S2A, Supporting Information, an average size of 0.5–3  $\mu\text{m}$  in primary particles is discernible in the view of SEM images. The features of NLMFO morphologies are comparable to NLMO and are presented in **Figure 1C**, Figures; S1D, and S2B, Supporting Information, while there are more particles whose dimensions are larger than 2.5  $\mu\text{m}$  in NLMFO than those in NLMO, and an average size of 1–6  $\mu\text{m}$  in primary particles are obtained. The NLMFO particles are more inclined to aggregate and grow rapidly than NLMO particles during thermal treatment. Transmission Electron Microscopy (TEM) was employed to observe microstructures. As **Figure 1B,F** shows, the prepared particles of NLMO and NLMFO are not perfect single crystals but are composed of stacked layers along with diverse directions, which could be regarded as quasi-single crystals.<sup>[31]</sup> The corresponding energy dispersive spectroscopy mapping results are presented in **Figure S1**, Supporting Information, Na, Mn, and O elements are distributed uniformly throughout the particles. The even distribution of iron element further confirms the uniform doping of iron.

XRD measurements were carried out to characterize the crystal structures. The XRD patterns of the two types of samples could be fully indexed to the space group of  $P6_3/mmc$  (No. 194), indicating that NLMO and NLMFO are typical P2-type hexagonal structures with no impurity phases. Rietveld refinement results of two samples are shown in **Figure 1E,F**, the values of reliability factors R-pattern ( $R_p$ ) and R-weighted pattern ( $R_{wp}$ ) are both relatively low, and the goodness of fit is less than 2, suggesting high accuracy of the structure models and the atom sites of the Rietveld refinements. The lattice parameters of the refinement results are shown in **Tables S1 and S2**, Supporting Information. Inductively Coupled Plasma-Mass Spectroscopy (ICP-MS) analysis was employed to quantify the contents of elements further. The raw results are presented

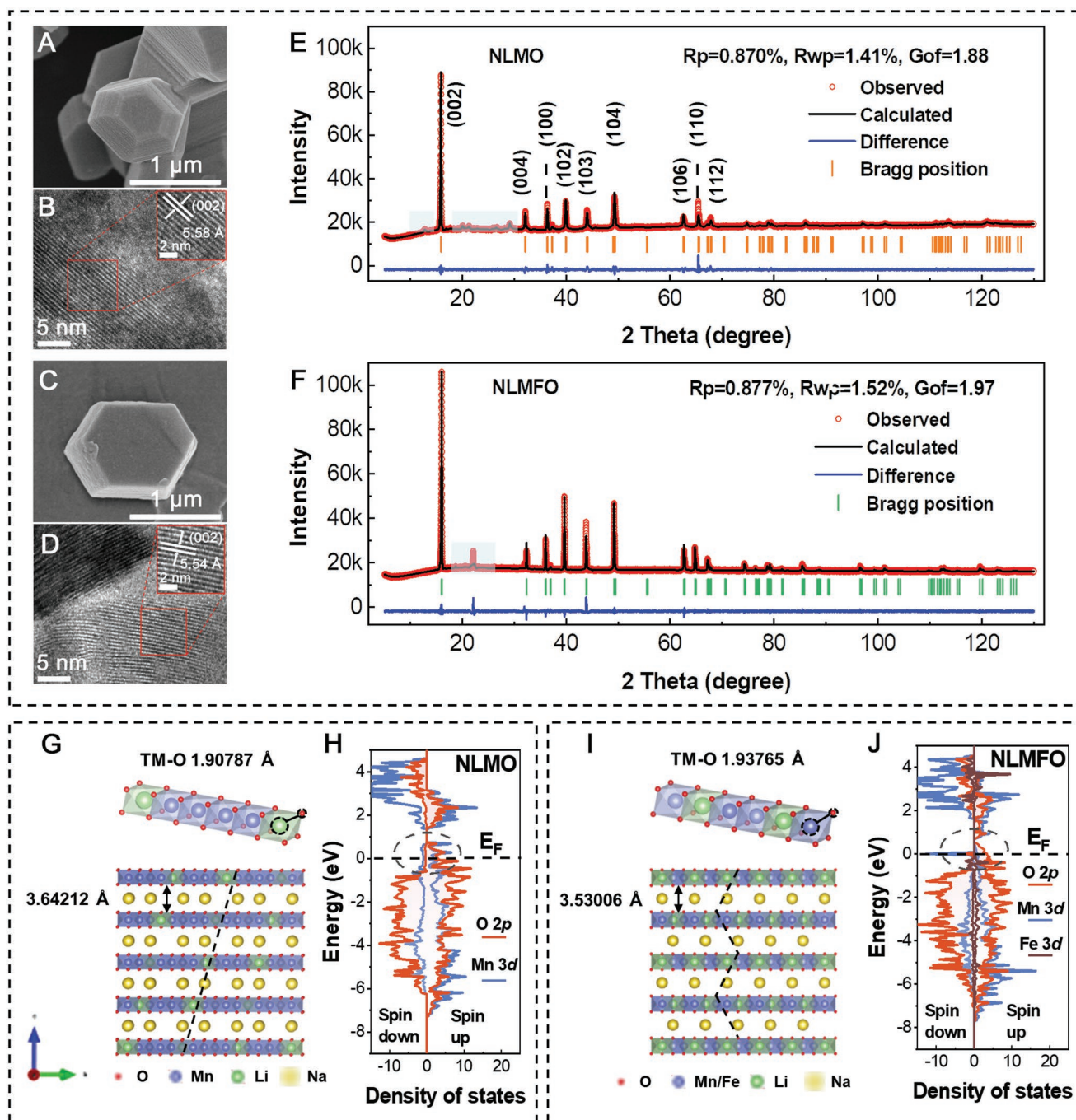


**Figure 1.** Physical characterization, structural diagram, and DFT calculations of NLMO and NLMFO. A–D) SEM images and HRTEM images of NLMO and NLMFO samples, respectively. E–F) Rietveld refinement of the X-ray powder diffraction data for NLMO and NLMFO, respectively. G, I) Variation of intra-layer O-TM bond distance and inter-layer of sodium layer bond distance due to doping by iron. H, J) Spin resolved pDOS of NLMO and NLMFO, respectively.

in Table S3, Supporting Information and confirm that the chemical formulas of NLMO and NLMFO are  $\text{Na}_{0.53}\text{Li}_{0.19}\text{Mn}_{0.82}\text{O}_2$  and  $\text{Na}_{0.56}\text{Li}_{0.218}\text{Mn}_{0.753}\text{Fe}_{0.07}\text{O}_2$  respectively, which are consistent with the results obtained by the XRD Rietveld refinements. Figure 1B,D shows interlayer distances between neighboring lattice fringes. The 5.58 and 5.54 Å correspond to the d-spacing values of (002) plane of NLMO and NLMFO, which

are close to the results obtained by XRD Rietveld refinements. It is worth noting that there are some minor peaks between  $20^\circ$  and  $30^\circ$  in the XRD patterns of NLMO, which evidently demonstrate the ribbon-ordered arrangement of Li/Mn in NLMO.<sup>[24]</sup> We performed characteristic peaks simulation of ribbon-ordered supercell (...Li-4Mn-Li...) using VESTA, the model with  $-\alpha\beta$ -configuration is presented in Figure S3, Supporting

Information. It is unambiguously clear that the calculated profile agrees well with the experimental data. On the basis of simulation, diffraction peaks at 12.81°, 20.05°, 21.30°, 26.77°, and 29.04° can be indexed as (200), (111), (11 $\bar{1}$ ), (311), ( $\bar{3}$ 11) planes, respectively, for superstructure in the NLMO we synthesized. As for NLMFO, the original ribbon-ordered superstructure was not identified anymore, but the honeycomb-ordered superstructure was more inclined to form as confirmed by the diffraction peaks at 22°. [16] To further confirm the resulting superstructure, we also employed VESTA to simulate  $\sqrt{3}a \times \sqrt{3}a$ -type supercells, and the calculated XRD profile based on a model composed of AB-type stacking sequences could be matched reasonably well with the experimental results (Figure S3E, Supporting Information). Considering that the synthesis conditions are identical, except for the appearance of Fe<sub>2</sub>O<sub>3</sub> in the precursor, we infer that the presence of Fe<sup>3+</sup> ions should enable the superstructure to be apt to transform into the honeycomb-ordered superstructure. Therefore, we employed DFT calculations to investigate the total energy of NLMFO composed of different superstructures, and the results are presented in Figure S4, Supporting Information. If the ribbon-ordered superstructure is maintained after iron doping into the ribbon-ordered NLMO, the total energy would be 15 meV/f.u. lower. However, when the superstructure transfer to honeycomb-ordered, the total energy is 39 meV/f.u. lower than ribbon-ordered NLMO. For this result, the NLMFO with honeycomb-ordered superstructure is more inclined to be obtained and more stable. Hence, it's easier for the crystal nucleus of NLMFO to grow up and merge into bigger crystals under the same thermal treatment, which explains why the NLMFO particles are a little bigger than the NLMO particles. Except for the effect on the superstructure, the distinction in crystals' structure symmetry and degree of order could also be seen from Raman spectroscopic measurements. As Figure S5, Supporting Information exhibits, the Raman response of pristine NLMO shows typical peaks  $\approx$ 643 and 579 cm<sup>-1</sup>, which could be assigned to A<sub>1g</sub> stretching mode and E<sub>g</sub> bending mode, respectively. [32–33] The characteristic peaks of NLMFO are located around 590 cm<sup>-1</sup>, which could be ascribed to A<sub>1g</sub> mode, and a lower peak at 612 cm<sup>-1</sup> could be regarded as E<sub>g</sub> mode. The A<sub>1g</sub> mode is related to stretching vibrations from the out-of-plane TM–O layers parallel to the *c* axis. The E<sub>g</sub> mode is associated with atomic displacements perpendicular to the *c* axis, corresponding to in-plane O–TM–O bending. [34–35] Compared with NLMFO, the shift of A<sub>1g</sub> mode in NLMO toward a higher wave number could be ascribed to a larger *c*-axis parameter, which is also obtained by XRD Rietveld refinements. More apparently, the NLMO has a narrower full width at half maximum, indicating a higher level of symmetry and better-ordered atom arrangements. [32,36]

On the basis of reliable XRD Rietveld refinements results, we investigated the variation of bond length among the two materials. The introduction of iron into the bulk of NLMO, results in an elongation of the TM–O bond length along the axial direction, as illustrated in Figure 1G,I. The change in the TM–O bond length from 1.895 to 1.951 Å can be attributed to the fact that the ionic radius of Fe<sup>3+</sup> ions (0.64 Å) is larger than that of the Mn<sup>4+</sup> ions (0.53 Å). Considering this alteration, we predicted performance changes resulting from doping by iron, in light of previous reports. [10,29,37–38] With the TM–O bond

prolongation, the overlap between TM *d* orbitals and O *2p* orbitals decreases, the hybridization becomes weaker, which can enable much more lattice oxygen atoms to participate in charge compensation interactions. Also, some irreversible reactions could take place as well because of these structural changes.

DFT calculations were also performed to explore changes in bands interaction between oxygen *2p* orbitals and TM *d* orbitals, in order to verify our prediction. Figure 1H,J illustrates the partial density of states (pDOS) of NLMO and NLMFO, respectively. Indeed, it can be clearly observed within the black dotted circle, there is a reduction in the overlap between O and Mn bands due to doping by Fe atoms. O *2p* bands dominate the DOS in the vicinity of the E<sub>f</sub>, suggesting that much more O atoms are capable of participating in charge compensation interactions during cycling. A similar conclusion also can be drawn from the results of X-ray photoelectron spectroscopy (XPS), related to the Mn *2p* orbitals. As Figure S6, Supporting Information shows, the peaks of Mn *2p* related to NLMFO are shifted by around 0.3 eV to lower energy. This can be ascribed to the weakening of the band interactions, since electrons of Mn atoms are subjected to less constrains from the lattice oxygen atoms. In summary, the above-described spectroscopic results are in good agreement with our inference based on the variation of the TM–O bonds' length. On top of the above-mentioned effects, we noticed that the bandgap between the top of the oxygen bands and the bottom of the conduction band contracts due to doping by Fe atoms, which might make it easier for the oxygen atoms to exchange electrons, thus facilitating their possible involvement in charge transfer processes.

## 2.2. Electrochemical Performance of NLMO and NLMFO Electrodes

Cyclic voltammetry tests were performed to study the redox peaks of the two types of materials within different potential windows. As shown in Figure S7, Supporting Information, in the potential range of 1.9–4.4 V, NLMO electrodes have prominent and strong peaks at  $\approx$ 4.2 and 2.2 V corresponding to the oxygen and manganese redox interactions, respectively. [27,39] In contrast, the redox peaks of NLMFO electrodes are broad and seemingly distributed among the entire potential window, which might be due to voltage hysteresis. [40] As we broadened the potential range to 1.5–4.7 V, the oxidation reactions of the oxygen moieties are more completed, and the original oxygen reduction peak located at 4.09 V is shifted to 3.6 V, indicating that excessive oxygen reactions lead to a certain degree of voltage hysteresis with NLMO electrodes. In turn, with NLMFO electrodes the position of oxygen reduction peak does not change, but its intensity increases, which can be ascribed to a higher level of lattice oxygen atoms involvement in redox reactions. The capacity–voltage curves within different potential windows are presented in Figure S8, Supporting Information. We can see that the polarization increases with the cutoff voltage exceeding 4.4 V. Notably, a more obvious voltage hysteresis and rapid voltage decay in the discharge voltage plateau can be observed with NLMO electrodes. In contrast, the sequential

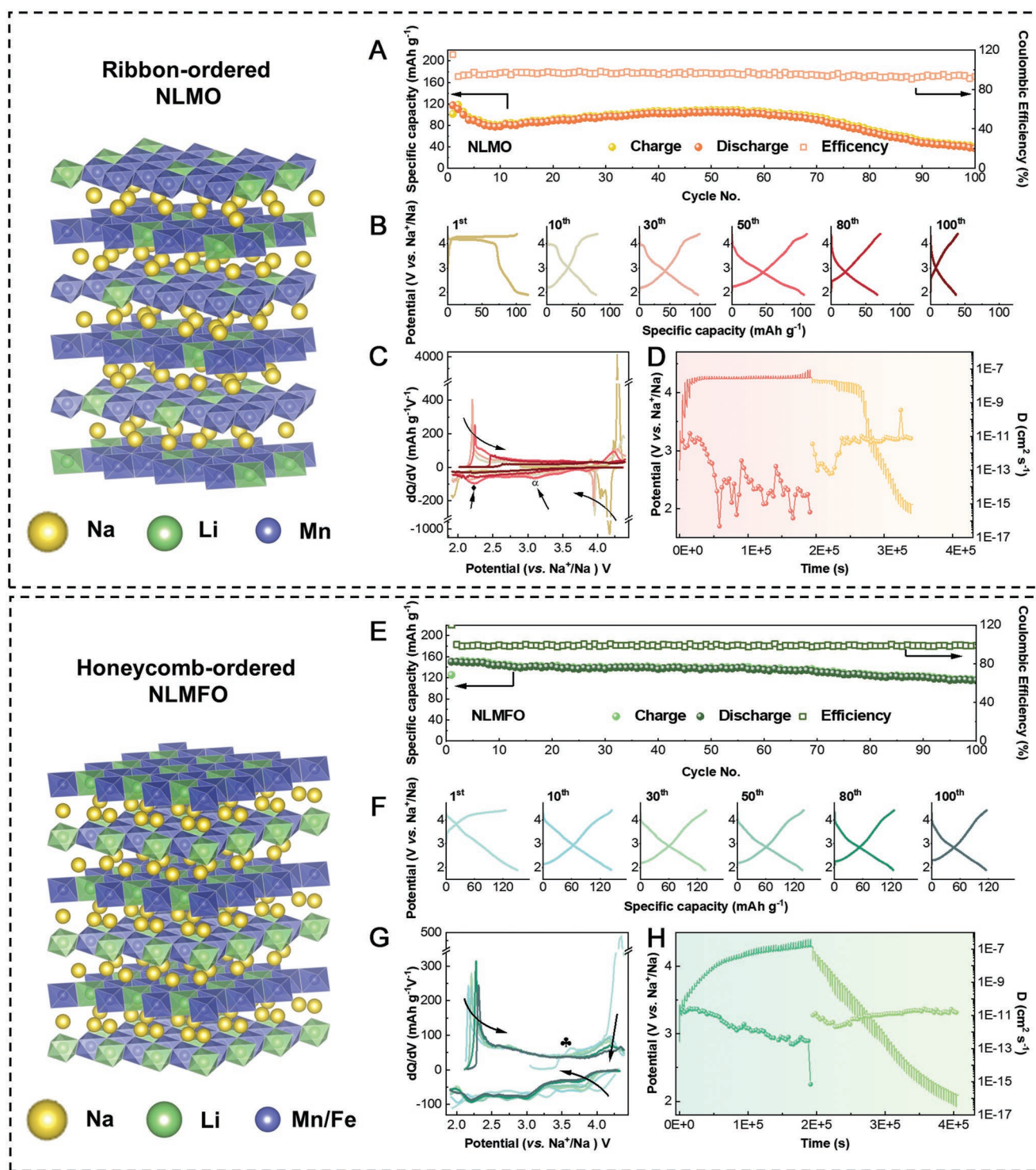


**Figure 2.** Electrochemical performances of NLMO and NLMFO. A,E) Cycle performances of ribbon-ordered NLMO electrodes and honeycomb-ordered NLMFO electrodes over 100 cycles. B,F) The capacity-voltage curves for different cycles of NLMO and NLMFO electrodes upon cycling between 1.9 and 4.4 V at 20 mA g<sup>-1</sup>. C,G) The dQ/dV versus V plots corresponding to the (B) voltage profiles of NLMO electrodes and (F) NLMFO electrodes. D,H) GITT curves and calculated diffusion coefficients of the Na ions for the first cycle of NLMO and NLMFO electrodes.

voltage profiles in the charts of Figure S8, Supporting Information are similar, and clearly reflect the much higher stability of NLMFO electrodes.

To obtain a more stable cycling performance and eliminate factors of electrolyte oxidation on the electrodes, a potential window of 1.9–4.4 V was employed to measure long cycling

performances. In previous reports, researchers focused on the first 20 cycles of P2-NLMO electrodes (with  $-\alpha\beta$  configuration) to study the root of degradation in the electrochemical performance upon cycling. Here, we extended these tests to 100 cycles and found variations in the capacity-voltage curves and improvement in the discharge capacity. The cycling performance of these electrodes is shown in Figure 2A, and the capacity-voltage curves of the 1<sup>st</sup>, 10<sup>th</sup>, 30<sup>th</sup>, 50<sup>th</sup>, 80<sup>th</sup>, and 100<sup>th</sup> cycles are presented in Figure 2B. In the first cycle, NLMO electrodes deliver a discharge capacity of 117 mA h g<sup>-1</sup>, including a specific capacity of around 68 mA h g<sup>-1</sup> with a long plateau above 4.0 V that is contributed by the ribbon-ordered superstructure. Considering the initial charge capacity of 101.2 mA h g<sup>-1</sup>, the coulombic efficiency of the first cycle hits 115%. The phenomenon can be ascribed to sodium-poor pristine materials caused by a loss of sodium under the high-temperature calcination upon the synthesis.<sup>[18]</sup> After ten cycles, the charge and discharge platforms at high voltage gradually disappear, accompanied with a plummeting to a capacity of 77.9 mA h g<sup>-1</sup>. Hu et al.<sup>[25]</sup> revealed the origin of the performance degradation and proposed that the irreversible interlayer stacking transformation from  $-\alpha\beta$  to  $-\alpha\gamma$  sequences during successive charge and discharge processes is responsible for the poor performance. The discharge capacity progressively recovers after 10 cycles and increases to 104.8 mA h g<sup>-1</sup> at 50 cycles, with the capacity-voltage curves evolving into S-shaped curves. The decrease in plateau region can be attributed to less oxygen redox or possible voltage hysteresis. The slope region between 2.0 and 3.5 V becomes wider and wider, which has been found in previous reports and has been ascribed to the activation of Mn<sup>4+</sup>/Mn<sup>3+</sup> to compensate for capacity loss from O<sub>2</sub><sup>n-</sup>/O<sub>2</sub><sup>2-</sup>.<sup>[41–42]</sup> After 60 cycles, the discharge capacity decays accompanied with increasing polarization, and only 37.1 mA h g<sup>-1</sup> is left after 100 cycles, corresponding to a capacity retention of 33.6%.

Due to the iron introduction prefers the formation of honeycomb-ordered superstructure. The capacity-voltage curves of NLMFO exhibit considerable stability throughout the entire cycle. Figure 2E,F displays the cycling performance and voltage profiles of NLMFO, respectively. The initial charge capacity of the first cycle is 125.4 mA h g<sup>-1</sup>. Because all the Mn is +4 valence in NLMO and NLMFO, the cooperation of Fe<sup>4+</sup>/Fe<sup>3+</sup> redox pair and LOR in NLMFO could provide 24.2 mA h g<sup>-1</sup> more capacity than solely relying on LOR in NLMO. As for the quantitative analysis of specific capacity contribution, we will discuss it in the charge compensation part. Owing to iron introduction, the initial discharge capacity achieves 150.4 mA h g<sup>-1</sup>. The capacity retention ratios of 60 and 100 cycles reach 90.27% and 77%, respectively. Acceleration of properties degradation after 60 cycles can be ascribed to accumulation of side reaction productions and particles fragmentation.<sup>[27,40]</sup>

The differential capacity (dQ/dV vs V) curves of NLMO are presented in Figure 2C to understand electrochemical behaviors evolution. Each curve corresponds to the voltage profile with the same color in Figure 2B. An extremely high anodic peak in the initial charging process appearing at 4.27 V, corresponds to the combination of oxygen evolution and possible electrolyte solution decomposition.<sup>[17,43]</sup> This peak becomes significantly lower in the following cycles while the other anodic peak located below 2.5 V corresponding to the oxidation of Mn

is steady in position and intensity during the first 50 cycles. The shift of the manganese redox center is likely due to structural change caused by oxygen evolution and other accompanying structural reorganization of the lattice.<sup>[43]</sup> The strong cathodic peak located at 4.17 V can be attributed to the reduction of peroxide/superoxide-like species, along with some smaller peaks below 4.1 V, whose assignments cannot be clarified yet. Upon successive cycles, the reduction peak at 4.17 V shifts to lower voltages and becomes narrower and weaker, signifying that the characteristic high discharge voltage plateau related to the ribbon-ordered superstructure gradually disappears. After 50 cycles, a new small reduction peak emerges at around 3.1 V, guided by a black spade. This peak can be ascribed to the oxygen reduction process with voltage hysteresis. The low potential cathodic peak at 2.25 V pointed by a black diamond-shaped mark refers to Mn<sup>4+</sup>/Mn<sup>3+</sup> reduction, indicating the activation of Mn<sup>4+</sup>/Mn<sup>3+</sup> to compensate for the capacity loss. In contrast to the drastic change in capacity-voltage curves of NLMO electrodes during cycling, the NLMFO electrodes with the honeycomb-ordered superstructure exhibit great stability after the first cycle. It is worth noting that a small anodic peak at 3.63 V pointed with a club mark corresponds to the Fe<sup>4+</sup>/Fe<sup>3+</sup> redox process. The capacity-voltage curves are continuously changing with discharge voltage decay and increasing polarization, but without great differences compared to the initial cycle. It can also be seen from the discharge mid-voltage evolution with cycles in Figure S9, Supporting Information that the discharge potential of NLMO shows a pronounced decrease from 4.07 to 2.87 V during the first 10 cycles and decays slowly in subsequent cycles. With NLMFO electrodes, the voltage decay observed during long cycling experiments is much lower compared to what can be observed with NLMO electrodes. The discharge mid-voltage for NLMFO electrodes decreases from 2.91 V to 2.701 after 100 cycles, while for NLMO electrodes, the discharge mid-voltage after 100 cycles is only 2.52 V, suggesting the higher stability of NLMFO during a long cycling test.

Galvanostatic intermittent titration technique (GITT) was applied to further evaluate the reaction kinetics and ions transport properties. Figure 2D depicts the charge/discharge GITT curves of NLMO electrodes during the first cycle at 10 mA g<sup>-1</sup>. The minimum Na<sup>+</sup> ions diffusion coefficient ( $D_{\text{Na}^+}$ ) appears at the oxygen oxidation state, which is similar to previous reports.<sup>[37]</sup> The corresponding average value of  $D_{\text{Na}^+}$  among oxygen redox is only  $1.5 \times 10^{-14}$  cm<sup>2</sup> s<sup>-1</sup>. Figure 2H illustrates the GITT curves of NLMFO electrodes. It also exhibits a decrease in the Na<sup>+</sup> ions diffusion coefficient in the high voltage region where the lattice oxygen atoms participate in the charge compensation process. However, the whole ions mobility performance of NLMFO is better than that of NLMO, which can be attributed to the faster electron transfer that has been proved by the pDOS calculations and ligand-to-metal charge transfer process (LMCT) by the formation of Fe 3d-O 2p delocalized state. Figure S10 shows the ions mobility properties after 55 cycles. For NLMO electrodes, manganese atoms participate in the charge compensation at the low potential region, corresponding to a  $D_{\text{Na}^+}$  of  $6.2 \times 10^{-12}$  cm<sup>2</sup> s<sup>-1</sup>. A small amount of oxygen atoms is involved in the charge compensation process, as can be inferred from the decrease in the mobility of the ions at the high potential domain. For NLMFO electrodes, the

migration of ions is much better. This can be ascribed to better interfacial interactions of these electrodes (they are stabilized by doping with Fe) and their reductive coupling mechanism.<sup>[44]</sup>

Furthermore, rate performance data are presented in Figure S11, Supporting Information to confirm the reversibility of oxygen redox reaction. Considering the boosted capacity in NLMFO, we subjectively set the current density of 1 C as 100 mA g<sup>-1</sup> and 150 mA g<sup>-1</sup> for NLMO and NLMFO, respectively, to accurately evaluate the rate performance. The NLMFO exhibits an outstanding rate performance compared to NLMO, a 68.07% capacity can be maintained in the current density of 2 C, corresponding to a capacity of 103.2 mA h g<sup>-1</sup>. While as for NLMO, the oxygen redox is prominently inhibited in high current density, which can be ascribed to the inherent sluggish oxygen redox reaction kinetics, and the capacity retention ratios are only 51.46%, 39.09%, 32.33%, and 26.20%, when the current density are 0.2, 0.5, 1, and 2 C, respectively. The improved charge transfer capability due to the narrower bandgap and LMCT process,<sup>[45]</sup> as well as faster ions transport properties all contribute to the better rate performance and higher reversibility of oxygen redox reaction of NLMFO.

### 2.3. Evolution of Structures in NLMO and NLMFO Electrodes Upon Cycling

To understand the correlation between the electrochemical behavior change and structure evolution during cycling, we performed in situ XRD measurements to precisely follow their structural evolution as the electrochemical processes prevail. The corresponding contour plots of peaks evolution for NLMO and NLMFO electrodes are shown in Figure 3A,D, along with cell voltage profiles as a function of time (left). Because characteristic diffraction peaks of the superstructure are too weak, it could not be easy to detect them during these in situ XRD measurements. In the XRD patterns of NLMO electrodes, during the first charging process, the intensity of (002) diffraction peak gradually decreases without a prominent change in peak position. Instead, a broad and low-intensity diffraction peak (relates to disordered structure) neighboring the right of (002) peak emerges. Similarly, the intensity of the (100) peak diminishes during the charging process, replaced by an obvious wide diffraction peak located at a higher angle (related to disordered material). These results are consistent with the observations reported previously.<sup>[26]</sup> Sung et al. regarded the new phase structure as the “Z” phase and explained that the broad diffraction peaks (reflecting amorphization) are caused by stacking faults induced by a two-phase reaction. The two phases are composed of different vacancy/Na arrangement coordination and it is induced by the LOR. In the subsequent discharge process, both intensities and positions of peaks return to their original states. As the voltage profiles transfer into S-shaped, these broad diffraction peaks vanish during the test. Ex situ XRD patterns at different states of charge are presented in Figure S12, Supporting Information to characterize the structure variation more distinctively. After 50 cycles, the electrochemical behavior manifests a complete disappearance of the high potential plateau. The crystal structure exhibits excellent stability during the entire charge and discharge process, as revealed by XRD.

Different from the above description, with NLMFO electrodes the position of (002) peak shifts to a lower angle without an obvious decrease in intensity. With the extraction of sodium ions, interlayer spacing along the c-axis orientation expands due to the increase of electrostatic repulsion between adjacent layers of lattice oxygen atoms. The well-preserved intensity indicates that the ordered layers stacking of the (002) crystal facets are well preserved. On the other hand, the peaks related to the (100) crystal facets which reflect an ordered arrangement of the a–b planes also reasonably maintain their initial intensity. The (100) peak shifts to a higher angle due to the decrease of lattice parameters of a and b, which could be assigned to the oxidation of TM ions. The lattice parameters variation during the in situ XRD tests are presented in Figure S13, Supporting Information. As it shows, the lattice parameters change ratios of NLMFO are higher than those in NLMO. For NLMO, the a-axis and c-axis parameters only change 0.0052 and 0.0026 Å during the cycle, respectively. We think it can be attributed to the stacking faults. Notably, there is an abrupt change in parameters of NLMO within the blue region, corresponding to a step in the discharge curve, confirming the two-phase reaction during the first cycle. Differently, all the lattice parameters change of NLMFO show the characteristics of a single phase reaction. The evolution behaviors of peaks are almost reversible and the overall positions and intensities of the peaks are consistent with the initial states. The excellent reversible structural stability during cycling corresponds to an outstanding long cycling performance, which is well reflected by the stability of all the features in the electrochemical response of the iron-doped electrodes upon cycling.

### 2.4. Lithium Migration in NLMO and NLMFO

As lithium plays a crucial role in the activation of the oxygen redox behavior, it is critical to investigate the states of lithium in different cycles. Solid-state <sup>7</sup>Li NMR spectroscopy is sensitive to the local lithium environments, whether in crystalline or noncrystalline regions, as reported for a number of LIBs and SIBs.<sup>[46–48]</sup> Thus, we conducted <sup>7</sup>Li NMR measurements to follow the changes of lithium atoms in the electrode materials explored herein. Figure 4A,B shows the <sup>7</sup>Li spectra of NLMO and NLMFO taken from electrodes at different stages of cycling. The spectral features around 2060 ppm can be ascribed to Li ions surrounded by six nearest neighboring Mn<sup>4+</sup> ions in the ribbon-ordered superstructure.<sup>[24]</sup> The adjacent features ≈2270 and 1845 ppm resonance could be attributed to lithium in distorted crystal structure with different unit cell parameters. In the pristine state of NLMFO, broad spectral features ≈1735 ppm can be assigned to Li ions in the honeycomb-ordered superstructure with Li(OMn)<sub>6</sub> coordination.<sup>[27,43]</sup> In previously reported P2-Na<sub>0.8</sub>Li<sub>0.12</sub>Ni<sub>0.22</sub>Mn<sub>0.66</sub>O<sub>2</sub>,<sup>[49]</sup> the broadening of the spectral features could be caused by a combination of anisotropic bulk magnetic susceptibility (ABMS) effects, temperature gradients, or structural disorder. The less symmetry of NLMFO was also reflected by the above-described Raman measurements. In addition, the unpaired electrons in high-spin Fe<sup>3+</sup> cations have strong dipolar-dipolar interactions with lithium. So we can ascribe the broad features in the NMR spectra of

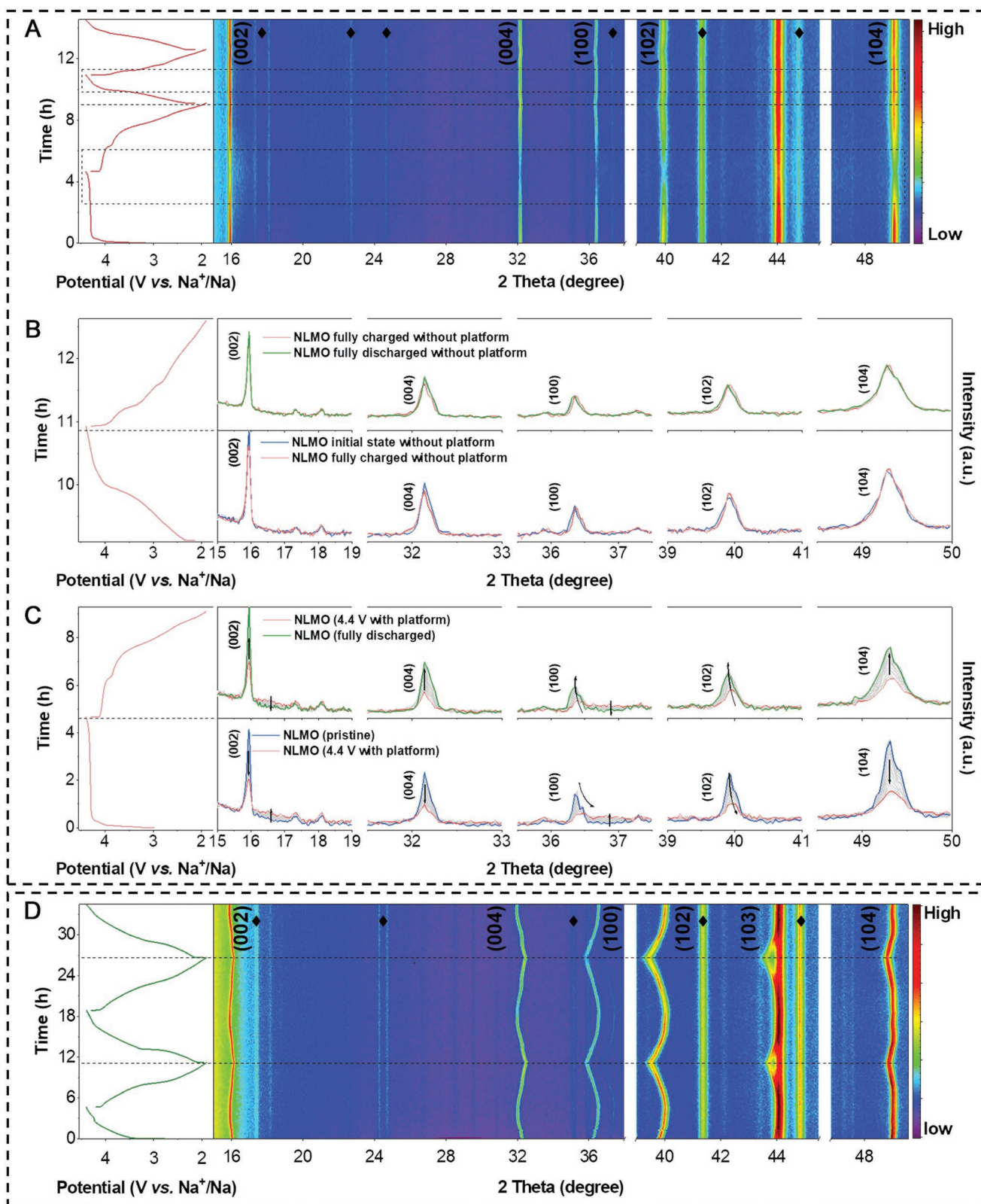


**Figure 3.** Time-resolved in situ XRD contours plots of A) NLMO and D) NLMFO electrodes during the first two full cycles and the third charge process. In situ XRD profiles collected during a cycle C) with a voltage plateau and a cycle B) without voltage plateau of NLMO electrodes in the vicinity of (002), (004), (100), (102), (104) peaks.



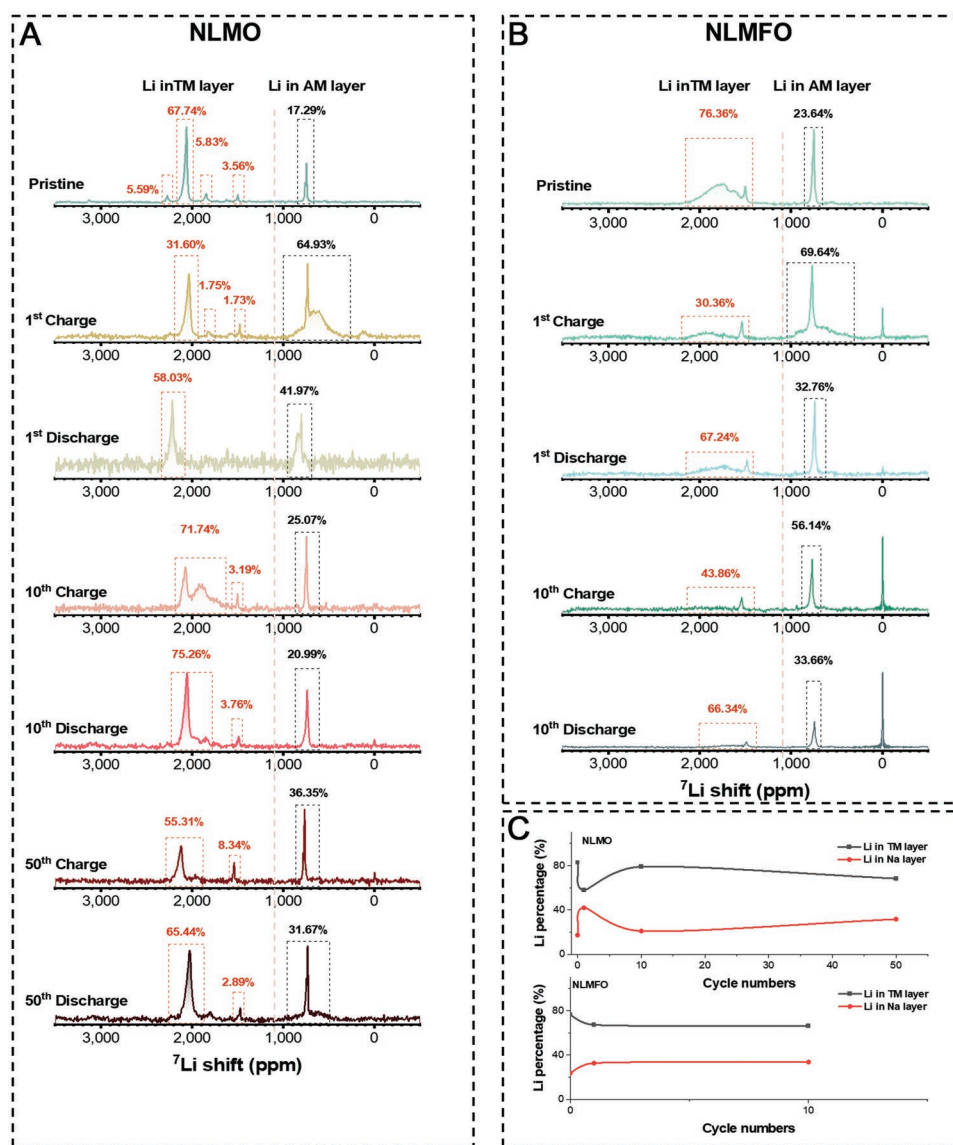


**Figure 4.** Ex situ solid-state  $^7\text{Li}$  nuclear magnetic resonance spectra of A) NLMO electrodes' samples at different states and B) NLMFO electrodes' samples at different states. C) Lithium percentage in TM layers and AM layers at different cycles. We mainly calculated the total Li content in the crystal structure.

NLMFO to the combination of ABMS and less symmetry in its structure. The shifts in 200–1000 ppm can be attributed to Li ions in sodium layers.<sup>[50]</sup> For both pristine samples, relative quantification based on the integral area of resonances proves that the content of lithium in the TM layers is much higher than that in the alkali metal (AM) layers. Such a distribution of lithium is desired and expected from our design principles. Due to the presence of lithium in the sodium layers in these localized regions, the coordination environment of Li ions distributed in TM layers is similar to that of Li ions in  $\text{Li}_2\text{MnO}_3$ . The minor peak observed at around 1500 ppm can be ascribed to the lithium in TM layers in these localized regions.

For NLMO, as the electrode is charged to 4.4 V and maintained for 10 min, the lithium content in well-ordered TM layers decreases to 31.6%, and the lithium content in sodium layers increases to around 65%, indicating that lithium

would migrate from TM layers to sodium layers at charged states, well consistent with previous reports. A new broadening of spectral features is observed between 400–900 ppm. The in situ XRD measurements detect the two-phase reaction at initially charged states, and Sung et al. have reported that the two-phase reaction is induced by different vacancy/ $\text{Na}^+$  coordination. Hence, the vacancy/ $\text{Na}^+$  coordination variation can result in disorder in the sodium layers (reflected by the broadened NMR features observed). Therefore, the above-mentioned broad spectral features can be assigned to lithium in disordered sodium layers. However, the environment of residual lithium in the TM layers does not change except for a slight shift to lower values, suggesting that the ordering of TM layers is well maintained and there is no strong dipolar-dipolar interaction between unpaired electrons and lithium. As the electrode is discharged to 1.9 V, the lithium in sub-crystalline

regions decreases, consistent with the structure reversibility observed by the in situ XRD measurements. As the electrode is charged to 4.4 V, at the 10th cycle, a new broad spectral feature is found between 1700–2200 ppm neighboring the original narrow peak. This change indicates a disordered arrangement of Li/Mn in localized regions in TM layers. In discharged state at the 10th cycle, the broad spectrum disappears, and a sharp peak is left with increased intensity, suggesting that the well-ordered arrangement of atoms is restored in the TM layers upon cycling. We can conclude that the NLMO would undergo Li/Mn coordination rearrangement in TM layers in charged states after several cycles, consistent with the transformation from  $\alpha\beta$  to  $\alpha\gamma$  sequences in the TM layers, as reported by Gu et al. At the same time, a drastic decrease in the discharge capacity with the disappearance of the plateau in the voltage profiles of NLMO electrodes, is observed in the 10th cycle. Accordingly, we attributed the capacity decay thus observed to the disordered arrangement of Li/Mn because disordered coordination can inhibit the oxygen redox activity, as reported previously.<sup>[51–53]</sup> At the 50th cycle, the electrochemical properties revert to better performance. Meanwhile, there is no sign that lithium is distributed in the sub-crystalline structure. The arrangement of atoms in the TM layers is ordered and steady no matter in charged or discharged states of the electrodes. It is worth noting that from these measurements we understand that more and more lithium is being trapped in sodium layers after the initial 10 cycles, but the migration of lithium between TM and sodium layers is rather reversible.

Regarding NLMFO, lithium initially in TM layers migrates to sodium layers in charged states and partially reverts in discharged states. The feature at 0 ppm can be assigned to diamagnetic species such as LiF or Li<sub>2</sub>CO<sub>3</sub>, which are formed on the surface due to possible side reactions between the active materials and solution species. According to the relative amount of lithium, the diamagnetic Li-containing species are produced more in the charged states. This could be attributed to reactions between metastable peroxide like moieties (formed by oxidation of active oxygen atoms, initially in an oxide state) with the electrolyte solution on the surface. Indeed it should be expected that NLMFO would produce more diamagnetic Li-containing species than NLMO due to the much higher redox activity of their oxygen atoms, as discussed throughout this manuscript, well supported by all the experimental results.

## 2.5. Charge Compensation Mechanism in NLMO and NLMFO

We have also investigated the charge compensation mechanism and the effect of the presence of iron on the redox behavior of the lattice oxygen atoms. The Ar etching assisted ex situ XPS measurements were implemented to identify oxygen-related species in the O 1s spectra, and Mössbauer spectroscopy, sensitive to the states of iron, was employed to detect the iron valence in NLMFO.<sup>[54–55]</sup> As shown in Figure 5A, both O 1s spectra of pristine states are composed of peaks at higher binding energy which could be assigned to surface oxygen deposits (carbonates/O=C=O and C–O), and a strong peak at the lower binding energy of 529.5 eV which could be ascribed

to O<sup>2-</sup> anions in the crystalline network. For a fully charged sample, a new oxygen peak at 530.5 eV is introduced to account for the asymmetry of lattice oxygen peaks.<sup>[56–57]</sup> This extra peak can be ascribed to the component of oxidized oxygen O<sub>2</sub><sup>n-</sup>, which is formed by oxidation of lattice oxygen atoms. It could be unambiguously seen that the ratio of O<sub>2</sub><sup>n-</sup> peak area over the entire O 1s spectra in NLMFO is much higher than that of NLMO, indicating that much more lattice oxygen atoms participate in the charge compensation interactions. Furthermore, the Mössbauer spectra of pristine and fully charged NLMFO exhibited in Figure 5B are very informative. In its pristine state of NLMFO, Fe<sup>3+</sup> high spin state ( $S = 5/2$ ) is confirmed by values of IS = 0.63 mm s<sup>-1</sup> and QS = 1.98 mm s<sup>-1</sup>. The pristine sample shows typical quadrupole splitting, indicating a single Fe<sup>3+</sup> valence state. For the fully charged state, both Fe<sup>3+</sup> and Fe<sup>4+</sup> moieties coexist. 82.5% iron species are Fe<sup>3+</sup> ions at a low spin state ( $S = 1/2$ , IS = 0.28 mm s<sup>-1</sup> and QS = 0.72 mm s<sup>-1</sup>) and 17.5% are Fe<sup>4+</sup> ions (IS = 0.05 mm s<sup>-1</sup> and QS = 0.38 mm s<sup>-1</sup>). The Fe<sup>3+</sup> low spin state is generated by large ligand-field splitting which can be attributed to the extraction of sodium ions or distortion of FeO<sub>6</sub> octahedra.<sup>[54]</sup> Considering that only 17.5% of Fe is detected to be oxidized to Fe<sup>4+</sup> and the total content of Fe is 0.07 which was confirmed by ICP test, the specific capacity from Fe<sup>4+</sup>/Fe<sup>3+</sup> redox pair could be calculated from Equation 1:

$$\text{Capacity} = nF/3.6M (\text{mA h g}^{-1}) \quad (1)$$

The capacity contributed by the Fe<sup>4+</sup>/Fe<sup>3+</sup> redox pair is around 3.6 mA h g<sup>-1</sup> only, suggesting that the extra capacity of NLMFO around 20 mA h g<sup>-1</sup> is obtained by the oxygen atoms redox activity. Considering the potential effect of superstructure change on oxygen redox activity, we assess the electrochemistry properties of honeycomb-ordered NLMO. As Figure S14, Supporting Information shows, the initial charge capacity of honeycomb-ordered NLMO is 108.9 mA h g<sup>-1</sup>, close to the initial charge capacity of ribbon-ordered NLMO and some other honeycomb-ordered NLMO reported before<sup>[17,43]</sup> (The sodium content is 0.6), indicating that the transformation of superstructure has no effect on capacity, only leading to the variation of voltage profiles. This proves that iron introduction to the NLMO can trigger much more oxygen atoms participating in the charge compensation interactions by prolonging the TM–O bond, secondly, the formation of Fe 3d–O 2p delocalized state could facilitate the charge transfer by the LMCT processes to improve the oxygen redox reaction kinetics. Correspondingly, we also performed in situ differential electrochemical mass spectrometry (DEMS) test of two samples and the patterns are shown in Figure S15, Supporting Information. It can be clearly distinguished that O<sub>2</sub> and CO<sub>2</sub> are produced with NLMO electrodes, within the voltage plateau region while being charged. This proves that the two-phase reaction can induce oxygen release, which is harmful to the lattice structure. For NLMFO electrodes, the release of O<sub>2</sub> is less compared to that for NLMO electrodes. However, due to the much higher lattice oxygen atoms activity of NLMFO cathodes, more peroxide species on the surface should react with alkyl carbonate solvent molecules and produce much more CO<sub>2</sub> at high voltage.<sup>[17,58]</sup> This drawback can be easily alleviated by using effective coatings in pretreatments.

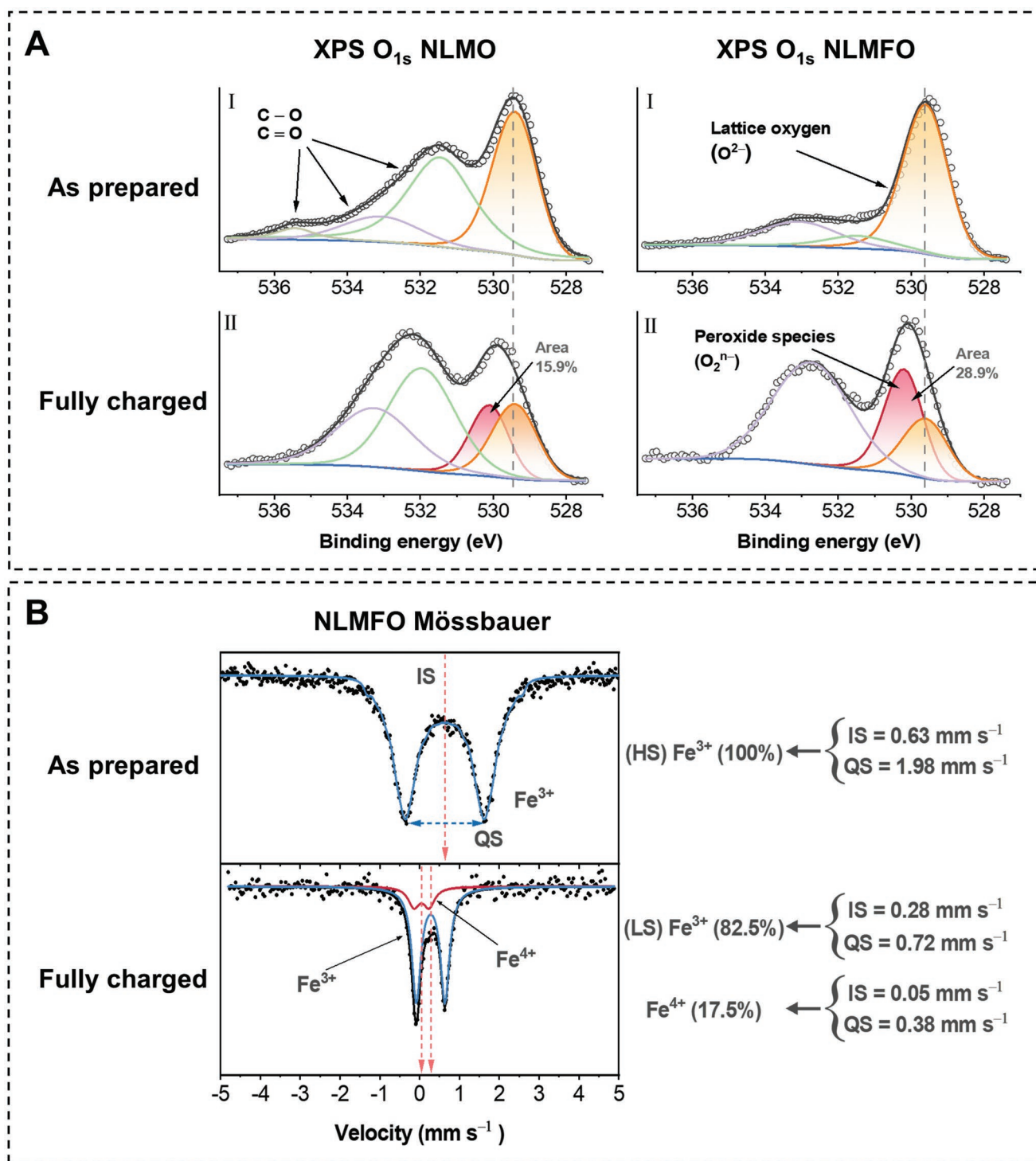


**Figure 5.** The ex situ Ar etching assisted XPS and Mössbauer spectra of NLMO and NLMFO. A) The Ar etching assisted XPS data related to O 1s peaks of as prepared and fully charged NLMO and NLMFO respectively. B) The <sup>57</sup>Co Mössbauer spectra of as prepared and fully charged NLMFO. Blue line: Fe<sup>3+</sup>; Red line: Fe<sup>4+</sup>.

### 3. Conclusion

In this work, we synthesized P2-type ribbon-ordered NLMO with a good crystalline structure and revealed that excessive

oxygen reaction within a relatively high voltage region should lead to a certain degree of voltage hysteresis. Then we evaluated long-term cycling performance of NLMO electrodes. After a plummeting in discharge capacities within the initial few cycles,

it gradually recovers back accompanied with a transformation of capacity-voltage curves into S-shape features. We performed in situ XRD and ex situ  $^7\text{Li}$  NMR to reveal different structural characteristics at different cycling states. For NLMO, we discover the disordered environment in sodium layers at first charged states. In situ XRD reveals that the change is induced by a reversible two-phase reaction composed of different vacancy/ $\text{Na}^+$  coordination arrangements, and the ordered atom sites in  $\text{Na}^+$  layers can be restored at the discharged states. Subsequently, due to the transformation from  $\alpha$ - $\beta$  to  $\alpha$ - $\gamma$  sequences in TM layers at initial cycles, a disorder in localized regions in the TM layers is found after 10 cycles and the severe decay of properties can be assigned to the localized disorder of the Mn/Li arrangement. After 50 cycles, a single-phase structure can be well preserved. Lithium is distributed in stable and ordered coordination arrangements, and the electrochemical behaviors have changed a lot. By doping NLMO with a small amount of iron, lower total energy induces the formation of honeycomb-ordered superstructure of NLMFO. Finally, we found that the introduction of iron into the structure pronouncedly enhances the involvement of lattice oxygen atoms in the redox activity of the cathode material, leading to a higher specific capacity. Due to the larger ionic radius of  $\text{Fe}^{3+}$ , the TM–O bond length can be prolonged. The interactions of O  $2p$  bands and TM  $3d$  bands are weakened, and thereby much more oxygen atoms are activated at high voltage, which is elucidated in detail by the combination of pDOS, Ar-etching XPS, and Mössbauer spectroscopies.

#### 4. Experimental Section

**Materials Synthesis:**  $\text{Na}_{0.6}\text{Li}_{0.2}\text{Mn}_{0.8}\text{O}_2$  was synthesized by high-temperature solid-state reaction using commercial  $\text{Na}_2\text{CO}_3$ ,  $\text{Li}_2\text{CO}_3$ , and  $\text{MnO}_2$  as precursors with an excess of 2 mol.%  $\text{Li}_2\text{CO}_3$  and 5 mol.%  $\text{Na}_2\text{CO}_3$  to compensate for the loss at high temperature. The powders were weighed in a stoichiometric proportion and ball-milled at 300 rpm in ethanol for 5 h, then dried overnight. The precursors were compacted in an  $\text{Al}_2\text{O}_3$  crucible and were heated at  $960\text{ }^\circ\text{C}$  for 16 h under an oxygen flow with a heating rate of  $5\text{ }^\circ\text{C min}^{-1}$ , then were cooled at  $2\text{ }^\circ\text{C min}^{-1}$  down to  $300\text{ }^\circ\text{C}$  and down to room temperature at a natural cooling speed. The obtained powder was rapidly ground and transferred to an argon-filled glovebox. The doped  $\text{Na}_{0.67}\text{Li}_{0.2}\text{Mn}_{0.73}\text{Fe}_{0.07}\text{O}_2$  was synthesized in the same method as above, while  $\text{Fe}_2\text{O}_3$  was added to the precursors mixture, as a source of iron, at the right proportion. The honeycomb-ordered NLMO was synthesized under  $700\text{ }^\circ\text{C}$  for 16 h in air atmosphere, employing the same precursor with ribbon-ordered NLMO.

**Materials Characterization:** The XRD measurements were conducted using Empyrean (Malvern Panalytical) in the  $2\theta$  range from  $5^\circ$  to  $130^\circ$  with a step range of  $0.0065^\circ$  and time per step of 1.872 s. The Rietveld refinements of the XRD patterns were operated by using the Fullprof software. Field emission scanning electron microscope (FESEM, Hitachi SU8010) was used to characterize the morphology of the various samples, and the particle sizes were measured with digital graph software. The micro nanostructure and images of lattice fringes were observed using a high-resolution transmission electron microscope (HRTEM, FEI Talos F200s) equipped with an energy-dispersive X-ray spectroscopy detector to analyze the distribution of elements. The schematic illustrations of the layered structures and superstructure models were obtained using VESTA software. ICP-MS was carried out to confirm the composition of samples using OPTIMA 8300. Raman spectra for pristine samples and electrodes were collected using a Horiba LabRAM HR Raman spectrometer with a laser of 532 nm wavenumber in an intensity of 10%.

**Electrochemical Methods:** The active materials powders, commercial carbon black, and polyvinylidene fluoride were mixed in appropriate amounts of N-methyl-2-pyrrolidinone in a weight ratio of 7:2:1 until the slurry was homogeneous. The mixing slurry was pasted on carbon-coated aluminum foils current collectors and dried at  $110\text{ }^\circ\text{C}$  in vacuum for 12 h. The thoroughly dried coated foils were rolled-pressed and punched into circular electrodes with a diameter of 12 mm, and an average mass loading of about  $1.77\text{ mg cm}^{-2}$ . The electrochemical performances of the electrodes were evaluated in coin-type cells (CR2032) assembled in an Ar-filled glove box. Porous glass fiber matrices (GF/D, Whatman) were used as separators. Metallic sodium foils were used as the negative electrodes. The electrolyte solution contained 1 M  $\text{NaClO}_4$  in ethylene carbonate/propylene carbonate (EC: PC, 1:1 in volume) with 5 vol.% of fluoroethylene carbonate. The galvanostatic charge and discharge test, long-term cycling performances, and rate properties were performed with CT2001A Land Battery computerized multichannel Test System in a voltage range of 1.9–4.4 V, besides, a current density of  $20\text{ mA g}^{-1}$  was applied when galvanostatic charge and discharge test and long-term cycling were performed. Cyclic voltammetry tests were conducted with a biological VMP-300 (EC-lab) computerized potentiostat system at a scan rate of  $0.1\text{ mV s}^{-1}$ . The GITT measurements were carried out at a constant current of  $10\text{ mA g}^{-1}$  for 10 minutes and followed by 50 minutes break to achieve quasi-equilibrium states with a biological VMP-300 (EC-lab) computerized potentiostat system. The Na ions diffusion coefficient ( $D_{\text{GITT}}$ ) was calculated based on Equation 2:

$$D_{\text{GITT}} = \frac{4}{\pi\tau} \left( \frac{m_{\text{B}}V_{\text{M}}}{M_{\text{B}}A} \right)^2 \left( \frac{\Delta E_{\text{S}}}{\Delta E_{\text{T}}} \right)^2 \quad (2)$$

**X-Ray Photoelectron Spectroscopy:** The XPS data were collected using KRATOS AXIS SUPRA. To avoid exposure in air, the fully charged electrodes were obtained by disassembling the coin cells in an Ar-filled glove box and were sealed to transfer to the XPS samples' chamber. The Ar ion beam etched the charged electrodes for around 100 s. The peaks were all calibrated using the C 1s core peak at 284.6 eV, and the full width at half maximum was restricted to the same value for peaks with the same color.

**Ex Situ Mössbauer Spectroscopy:** Mössbauer spectra of samples were acquired using  $^{57}\text{Co}/\text{Rh}$  system in a transmission geometry (WSSL-10 Wissel) at room temperature with a velocity of  $5\text{ mm s}^{-1}$ . Since the spectra intensity was proportional to the iron mass, electrodes used in this test were loaded to about  $7\text{ mg cm}^{-2}$ . Cells were charged at a current density of  $10\text{ mA g}^{-1}$  to 4.4 V and were held at 4.4 V for 10 min. Then the cells were disassembled in an Ar-filled glove box and the electrodes were washed with ethyl methyl carbonate solvent, before being measured.

**In Operando Differential Electrochemical Mass Spectroscopy (DEMS):** The analysis was performed with Pfeiffer Vacuum QMA410 system. A DEMS cell attachment was assembled in an Ar-filled glovebox. For each experiment, electrodes with a diameter of 12 mm containing  $2\text{ mg cm}^{-2}$  active mass was placed on top of the samples' attachment and the sodium tablet was placed at the bottom with Ar gas flow blowing from the top to accurately detect the generated gas. At the same time, a cell was cycled at a current density of  $10\text{ mA g}^{-1}$  in the range of 1.9 and 4.4 V. A cold trap cooled by carbon dioxide ice was used to avoid the volatilization of electrolyte components.

**In Situ XRD Analysis:** A special electrochemical cell for in situ XRD measurements was used, with a beryllium window that isolates the cell's contents from atmospheric contamination but is transparent to the X-ray that interact with the electrodes. The in situ XRD measurements were performed using an Empyrean (Malvern Panalytical) system with Cu  $K\alpha$  radiation ( $\lambda = 1.5406\text{ \AA}$ ) in  $2\theta$  range from  $10^\circ$  to  $60^\circ$ , with a step range of  $0.026^\circ$  and time per step of 0.3 s. The calculation of lattice parameters variation during in situ XRD was based on the Bragg equation and Equation 3:

$$d_{\text{hkl}} = \frac{1}{\sqrt{\frac{4}{3} \times \frac{(h^2 + hk + k^2)}{a^2} + \left(\frac{l}{c}\right)^2}} \quad (3)$$

**Solid-State  $^7\text{Li}$  Nuclear Magnetic Resonance measurements:** Ex situ solid-state NMR measurements were performed with a 600-MHz Bruker Advance III spectrometer with a  $^7\text{Li}$  Larmor frequency of 233.34 MHz in a 14.1 T magnetic field. To achieve high-resolution NMR spectra, the pjMATPASS pulse sequence was employed. LiCl aqueous solution with a  $^7\text{Li}$  chemical shift at 0.0 ppm was used as an external reference. For both samples, a 1.3 mm MAS probe was used and the rotors were spun at a MAS rate of 50 kHz. The applied  $\pi/2$  pulse length was 1.5  $\mu\text{s}$  and the recycle delay was 0.05 s. For each set of measurements, we prepared 6 electrodes with mass loading of around 4.8 mg  $\text{cm}^{-2}$ . After cycling, we dismantled the cells in an Ar-filled glove box and washed the electrodes with electrolyte solvent. We scrapped the powdery active material off the electrodes and ground it, then sealed it in a centrifuge tube for the NMR measurements.

**DFT Calculations:** We employed the Vienna ab initio simulation software package to achieve the density functional theory computations. The projector augmented wave method was also considered in these calculations. We first modeled supercells of  $\text{Na}_6\text{Li}_2\text{Mn}_8\text{O}_{20}$  and  $\text{Na}_6\text{Li}_2\text{Mn}_7\text{FeO}_{20}$  based on the results of VESTA, the honeycomb-ordered  $\text{Na}_6\text{Li}_2\text{Mn}_8\text{O}_{20}$  was modeled by replacing all Fe ions with Mn ions. The cutoff energy was set to be 500 eV, and a  $2 \times 10 \times 2$  k-point sampling grid was used. The convergence tolerances of energy and force were less than  $1.0 \times 10^{-5}$  eV/atom and  $10^{-3}$  eV/Å. The total energy was corrected using the DFT-D2 method. Here, the Hubbard U potential was employed to describe the Coulombic electron interaction precisely, and use the U-J values of Mn and Fe as 4 and 5.3 eV, respectively. As for the calculation of total energy.

**VESTA Simulation:** The creation and analysis of the ideal model was finished by VESTA.<sup>[59]</sup> The basic structure was created according to the lattice parameters obtained by refinements. The structure cell had been redirected and a special position substitution of expected atoms was performed. The theoretical XRD data were obtained from the powder diffraction simulation of the above structural models. The diffraction lines both of Cu- $K_{\alpha 1}$  and Cu- $K_{\alpha 2}$  were taken into account with an intensity ratio of 2:1.

## Supporting Information

Supporting Information is available from the Wiley Online Library or from the author.

## Acknowledgements

This work was supported by the National Natural Science Foundation of China (U1802256, 21773118, 21875107), Free Exploration Basic Research Project in Shenzhen Virtual University Park (2021Szvup062), Research and Practice Innovation Program in Nanjing University of Aeronautics and Astronautics (xcxjh20210603) and Priority Academic Program Development of Jiangsu Higher Education Institutions (PAPD).

## Conflict of Interest

The authors declare no conflict of interest.

## Authors Contribution

X.D.Q. and L.Y.W. contributed equally to this work. X.D.Q. and L.Y.W. designed the work. D.X.Q. and L.Y.W. carried out the experiment. X.D.Q., L.Y.W., Z.W.L., and K.S.H. evaluated the electrochemical performances. Y.N.L. performed the simulations. Y.X.X. carried out and analyzed the solid-state NMR data. X.D.Q. and L.Y.W. organized the figures and drafted the paper. E.Y. improve the language of the manuscript. D.A. and

X.G.Z. supervised the whole work. All authors contributed to the analysis and discussion of the data and revision of the paper.

## Data Availability Statement

The data that supports the findings of this study are available in the supplementary material of this article.

## Keywords

cycling performance, layered oxides, oxygen redox, sodium-ion batteries, superstructures

Received: July 12, 2022

Revised: August 24, 2022

Published online: September 28, 2022

- [1] M. Armand, J. M. Tarascon, *Nature* **2008**, 451, 652.
- [2] J. M. Tarascon, *Electrochem. Soc. Interface* **2016**, 25, 79.
- [3] H. Ren, Y. Li, Q. Ni, Y. Bai, H. Zhao, C. Wu, *Adv. Mater.* **2022**, 34, 2106171.
- [4] C. Vaalma, D. Buchholz, M. Weil, S. Passerini, *Nat. Rev. Mater.* **2018**, 3, 18013.
- [5] J.-Y. Hwang, S.-T. Myung, Y.-K. Sun, *Chem. Soc. Rev.* **2017**, 46, 3529.
- [6] C. Zhao, Q. Wang, Z. Yao, J. Wang, B. Sanchez-Lengeling, F. Ding, X. Qi, Y. Lu, X. Bai, B. Li, H. Li, A. Aspuru-Guzik, X. Huang, C. Delmas, M. Wagemaker, L. Chen, Y.-S. Hu, *Science* **2020**, 370, 708.
- [7] Q. Liu, Z. Hu, W. Li, C. Zou, H. Jin, S. Wang, S. Chou, S.-X. Dou, *Energy Environ. Sci.* **2021**, 14, 158.
- [8] I. Abate, S. Y. Kim, C. D. Pemmaraju, M. F. Toney, W. Yang, T. P. Devereaux, W. C. Chueh, L. F. Nazar, *Angew. Chem., Int. Ed.* **2021**, 60, 10880.
- [9] X.-L. Li, T. Wang, Y. Yuan, X.-Y. Yue, Q.-C. Wang, J.-Y. Wang, J. Zhong, R.-Q. Lin, Y. Yao, X.-J. Wu, X.-Q. Yu, Z.-W. Fu, Y.-Y. Xia, X.-Q. Yang, T. Liu, K. Amine, Z. Shadike, Y.-N. Zhou, J. Lu, *Adv. Mater.* **2021**, 33, 2008194.
- [10] H. Xu, S. Guo, H. Zhou, *J. Mater. Chem. A* **2019**, 7, 23662.
- [11] K. Luo, M. R. Roberts, R. Hao, N. Guerrini, D. M. Pickup, Y.-S. Liu, K. Edstrom, J. Guo, A. V. Chadwick, L. C. Duda, P. G. Bruce, *Nat. Chem.* **2016**, 8, 684.
- [12] D.-H. Seo, J. Lee, A. Urban, R. Malik, S. Kang, G. Ceder, *Nat. Chem.* **2016**, 8, 692.
- [13] Y. Yang, W.-F. Wei, *Rare Met.* **2020**, 39, 332.
- [14] M. M. Rahman, F. Lin, *Matter* **2021**, 4, 490.
- [15] X. Zhu, F. Meng, Q. Zhang, L. Xue, H. Zhu, S. Lan, Q. Liu, J. Zhao, Y. Zhuang, Q. Guo, B. Liu, L. Gu, X. Lu, Y. Ren, H. Xia, *Nat. Sustain.* **2021**, 4, 392.
- [16] N. Yabuuchi, R. Hara, M. Kajiyama, K. Kubota, T. Ishigaki, A. Hoshikawa, S. Komaba, *Adv. Energy Mater.* **2014**, 4, 1301453.
- [17] E. de la Llave, E. Talaie, E. Levi, P. K. Nayak, M. Dixit, P. T. Rao, P. Hartmann, H. F. Chesneau, D. T. Major, M. Greenstein, D. Aurbach, L. F. Nazar, *Chem. Mater.* **2016**, 28, 9064.
- [18] X. Rong, E. Hu, Y. Lu, F. Meng, C. Zhao, X. Wang, Q. Zhang, X. Yu, L. Gu, Y.-S. Hu, H. Li, X. Huang, X.-Q. Yang, C. Delmas, L. Chen, *Joule* **2019**, 3, 503.
- [19] Q. Li, Z. Yao, E. Lee, Y. Xu, M. M. Thackeray, C. Wolverton, V. P. Dravid, J. Wu, *Nat. Commun.* **2019**, 10, 5203.
- [20] B. Xiao, Y. Wang, S. Tan, M. Song, X. Li, Y. Zhang, F. Lin, K. S. Han, F. Omenya, K. Amine, X.-Q. Yang, D. Reed, Y. Hu, G.-L. Xu, E. Hu, X. Li, X. Li, *Angew. Chem., Int. Ed.* **2021**, 60, 8258.

- [21] G. Assat, J.-M. Tarascon, *Nat. Energy* **2018**, *3*, 373.
- [22] M. Sathiya, A. M. Abakumov, D. Foix, G. Rousse, K. Ramesha, M. Saubanere, M. L. Doublet, H. Vezin, C. P. Laisa, A. S. Prakash, D. Gonbeau, G. VanTendeloo, J. M. Tarascon, *Nat. Mater.* **2015**, *14*, 230.
- [23] Q. Wang, S. Mariyappan, G. Rousse, A. V. Morozov, B. Porcheron, R. Dedryvere, J. Wu, W. Yang, L. Zhang, M. Chakir, M. Avdeev, M. Deschamps, Y.-S. Yu, J. Cabana, M.-L. Doublet, A. M. Abakumov, J.-M. Tarascon, *Nat. Mater.* **2021**, *20*, 353.
- [24] R. A. House, U. Maitra, M. A. Perez-Osorio, J. G. Lozano, L. Jin, J. W. Somerville, L. C. Duda, A. Nag, A. Walters, K.-J. Zhou, M. R. Roberts, P. G. Bruce, *Nature* **2020**, *577*, 502.
- [25] A. Gao, Q. Zhang, X. Li, T. Shang, Z. Tang, X. Lus, Y. Luo, J. Ding, W. H. Kan, H. Chen, W. Yin, X. Wang, D. Xiao, D. Su, H. Li, X. Rong, X. Yu, Q. Yu, F. Meng, C. Nan, C. Delmas, L. Chen, Y.-S. Hu, L. Gu, *Nat. Sustain.* **2021**, *5*, 214.
- [26] S. M. Kang, D. Kim, K.-S. Lee, M.-S. Kim, A. Jin, J.-H. Park, C.-Y. Ahn, T.-Y. Jeon, Y. H. Jung, S.-H. Yu, J. Mun, Y.-E. Sung, *Adv. Sci.* **2020**, *7*, 2001263.
- [27] L. Yang, X. Li, J. Liu, S. Xiong, X. Ma, P. Liu, J. Bai, W. Xu, Y. Tang, Y.-Y. Hu, M. Liu, H. Chen, *J. Am. Chem. Soc.* **2019**, *141*, 6680.
- [28] B. Li, N. Jiang, W. Huang, H. Yan, Y. Zuo, D. Xia, *Adv. Funct. Mater.* **2018**, *28*, 1704864.
- [29] W. He, W. Guo, H. Wu, L. Lin, Q. Liu, X. Han, Q. Xie, P. Liu, H. Zheng, L. Wang, X. Yu, D.-L. Peng, *Adv. Mater.* **2021**, *33*, 2005937.
- [30] M. Kim, H. Kim, M. Cho, D. Kim, *J. Mater. Chem. A* **2021**, *9*, 15179.
- [31] R. Zhang, C. Wang, M. Ge, H. L. Xin, *Nano Lett.* **2022**, *9*, 3818.
- [32] M. Sendova-Vassileva, R. Stoyanova, D. Carlier, M. Yoncheva, E. Zhecheva, C. Delmas, *Adv. Sci. Technol.* **2010**, *74*, 60.
- [33] M. A. Khan, D. Han, G. Lee, Y.-I. Kim, Y.-M. Kang, *J. Alloys Compd.* **2019**, *771*, 987.
- [34] H. X. Yang, Y. Xia, Y. G. Shi, H. F. Tian, R. J. Xiao, X. Liu, Y. L. Liu, J. Q. Li, *Phys. Rev. B* **2006**, *74*, 094301.
- [35] R. E. Ruther, A. F. Callender, H. Zhou, S. K. Martha, J. Nanda, *J. Electrochem. Soc.* **2015**, *162*, A98.
- [36] M. Yoncheva, R. Stoyanova, E. Zhecheva, E. Kuzmanova, M. Sendova-Vassileva, D. Nihtianova, D. Cartier, M. Guignard, C. Delmas, *J. Mater. Chem. C* **2012**, *22*, 23418.
- [37] X.-L. Li, J. Bao, Z. Shadike, Q.-C. Wang, X.-Q. Yang, Y.-N. Zhou, D. Sun, F. Fang, *Angew. Chem., Int. Ed.* **2021**, *60*, 22026.
- [38] M. Ben Yahia, J. Vergnet, M. Saubanere, M.-L. Doublet, *Nat. Mater.* **2019**, *18*, 496.
- [39] E. J. Kim, P. A. Maughan, E. N. Basse, R. J. Clement, L. A. Ma, L. C. Duda, D. Sehwat, R. Younesi, N. Sharma, C. P. Grey, A. R. Armstrong, *Adv. Energy Mater.* **2022**, *12*, 2102325.
- [40] L. Yang, J. M. Lopez del Amo, Z. Shadike, S.-M. Bak, F. Bonilla, M. Galceran, P. K. Nayak, J. R. Buchheim, X.-Q. Yang, T. Rojo, P. Adelhelm, *Adv. Funct. Mater.* **2020**, *30*, 2003364.
- [41] K. Zhang, D. Kim, Z. Hu, M. Park, G. Noh, Y. Yang, J. Zhang, V. W.-h. Lau, S.-L. Chou, M. Cho, S.-Y. Choi, Y.-M. Kang, *Nat. Commun.* **2019**, *10*, 5203.
- [42] J. Jin, Y. Liu, Q. Shen, X. Zhao, J. Zhang, Y. Song, T. Li, X. Xing, J. Chen, *Adv. Funct. Mater.* **2022**, 2203424.
- [43] L. Yang, X. Li, X. Ma, S. Xiong, P. Liu, Y. Tang, S. Cheng, Y.-Y. Hu, M. Liu, H. Chen, *J. Power Sources* **2018**, *381*, 171.
- [44] Y. Zhang, M. Wu, J. Ma, G. Wei, Y. Ling, R. Zhang, Y. Huang, *ACS Cent. Sci.* **2020**, *6*, 232.
- [45] B. A. Li, K. Kumar, I. Roy, A. V. Morozov, O. V. Emelyanova, L. T. Zhang, T. Koc, S. Belin, J. Cabana, R. Dedryvere, A. M. Abakumov, J. M. Tarascon, *Nat. Mater.* **2022**, <https://doi.org/10.1038/s41563-022-01278-2>.
- [46] Y. J. Lee, F. Wang, C. P. Grey, *J. Am. Chem. Soc.* **1998**, *120*, 12601.
- [47] A. Van der Ven, M. K. Aydinol, G. Ceder, G. Kresse, J. Hafner, *Phys. Rev. B* **1998**, *58*, 2975.
- [48] W. Bowden, T. Bofinger, F. Zhang, N. Ilchev, R. Sirotina, Y. Paik, H. Chen, C. Grey, S. Hackney, *J. Power Sources* **2007**, *165*, 609.
- [49] J. Xu, D. H. Lee, R. J. Clement, X. Q. Yu, M. Leskes, A. J. Pell, G. Pintacuda, X. Q. Yang, C. P. Grey, Y. S. Meng, *Chem. Mater.* **2014**, *26*, 1260.
- [50] R. J. Clement, J. Xu, D. S. Middlemiss, J. Alvarado, C. Ma, Y. S. Meng, C. P. Grey, *J. Mater. Chem. A* **2017**, *5*, 4129.
- [51] L. Wang, T. Liu, A. Dai, V. De Andrade, Y. Ren, W. Xu, S. Lee, Q. Zhang, L. Gu, S. Wang, T. Wu, H. Jin, J. Lu, *Nat. Commun.* **2021**, *12*, 5370.
- [52] B. M. de Boisse, G. Liu, J. Ma, S.-i. Nishimura, S.-C. Chung, H. Kiuchi, Y. Harada, J. Kikkawa, Y. Kobayashi, M. Okubo, A. Yamada, *Nat. Commun.* **2016**, *7*, 11937.
- [53] X. Li, J. Xu, H. Li, H. Zhu, S. Guo, H. Zhou, *Adv. Sci.* **2022**, *9*, 2105280.
- [54] N. Yabuuchi, M. Kajiyama, J. Iwatate, H. Nishikawa, S. Hitomi, R. Okuyama, R. Usui, Y. Yamada, S. Komaba, *Nat. Mater.* **2012**, *11*, 512.
- [55] J. Zhao, L. Zhao, N. Dimov, S. Okada, T. Nishida, *J. Electrochem. Soc.* **2013**, *160*, A3077.
- [56] X. Rong, J. Liu, E. Hu, Y. Liu, Y. Wang, J. Wu, X. Yu, K. Page, Y.-S. Hu, W. Yang, H. Li, X.-Q. Yang, L. Chen, X. Huang, *Joule* **2018**, *2*, 125.
- [57] E. McCalla, A. M. Abakumov, M. Saubanere, D. Foix, E. J. Berg, G. Rousse, M.-L. Doublet, D. Gonbeau, P. Novak, G. Van Tendeloo, R. Dominko, J.-M. Tarascon, *Science* **2015**, *350*, 1516.
- [58] R. A. House, U. Maitra, L. Y. Jin, J. G. Lozano, J. W. Somerville, N. H. Rees, A. J. Naylor, L. C. Duda, F. Massel, A. V. Chadwick, S. Ramos, D. M. Pickup, D. E. McNally, X. Y. Lu, T. Schmitt, M. R. Roberts, P. G. Bruce, *Chem. Mater.* **2019**, *31*, 3293.
- [59] K. Momma, F. Izumi, *J. Appl. Crystallogr.* **2008**, *41*, 653.